Reflectance confocal microscopy of red blood cells: simulation and experiment

Adel Zeidan and Dvir Yelin[*]

Faculty of Biomedical Engineering, Technion—Israel Institute of Technology, Haifa 3200003, Israel
[*]yelin@bm.technion.ac.il

Abstract: Measuring the morphology of red blood cells is important for clinical diagnosis, providing valuable indications on a patient's health. In this work, we have simulated the appearance of normal red blood cells under a reflectance confocal microscope and discovered unique relations between the morphological parameters and the resulting characteristic interference patterns of the cell. The simulation results showed good agreement with *in vitro* reflectance confocal images of red blood cells, acquired using spectrally encoded flow cytometry that imaged the cells in a linear flow without artificial staining. By matching the simulated patterns to confocal images of the cells, this method could be used for measuring cell morphology in three dimensions and for studying their physiology.

©2015 Optical Society of America

OCIS codes: (170.1790) Confocal microscopy; (170.1470) Blood or tissue constituent monitoring; (170.1530) Cell analysis.

References and links

1. J. Ford, "Red blood cell morphology," Int. J. Lab. Hematol. **35**(3), 351–357 (2013).
2. M. Diez-Silva, M. Dao, J. Han, C.-T. Lim, and S. Suresh, "Shape and biomechanical characteristics of human red blood cells in health and disease," MRS Bull. **35**(5), 382–388 (2010).
3. J. Lim, H. Ding, M. Mir, R. Zhu, K. Tangella, and G. Popescu, "Born approximation model for light scattering by red blood cells," Biomed. Opt. Express **2**(10), 2784–2791 (2011).
4. R. Liu, D. K. Dey, D. Boss, P. Marquet, and B. Javidi, "Recognition and classification of red blood cells using digital holographic microscopy and data clustering with discriminant analysis," J. Opt. Soc. Am. A **28**(6), 1204–1210 (2011).
5. Y.-S. Choi and S.-J. Lee, "Three-dimensional volumetric measurement of red blood cell motion using digital holographic microscopy," Appl. Opt. **48**(16), 2983–2990 (2009).
6. E. M. Strohm, E. S. Berndl, and M. C. Kolios, "Probing red blood cell morphology using high-frequency photoacoustics," Biophys. J. **105**(1), 59–67 (2013).
7. E. M. Strohm, E. S. L. Berndl, and M. C. Kolios, "High frequency label-free photoacoustic microscopy of single cells," Photoacoustics **1**(3-4), 49–53 (2013).
8. W.-H. Kim, C.-I. Kim, S.-W. Lee, S.-H. Lim, C.-W. Park, H. Lee, and M.-K. Park, "Particle image velocimetry of the blood flow in a micro-channel using the confocal laser scanning microscope," J. Opt. Soc. Korea **14**(1), 42–48 (2010).
9. M. Rajadhyaksha, R. R. Anderson, and R. H. Webb, "Video-rate confocal scanning laser microscope for imaging human tissues in vivo," Appl. Opt. **38**(10), 2105–2115 (1999).
10. M. Rajadhyaksha, S. González, J. M. Zavislan, R. R. Anderson, and R. H. Webb, "In vivo confocal scanning laser microscopy of human skin II: advances in instrumentation and comparison with histology," J. Invest. Dermatol. **113**(3), 293–303 (1999).
11. W. M. White, M. Rajadhyaksha, S. González, R. L. Fabian, and R. R. Anderson, "Noninvasive imaging of human oral mucosa in vivo by confocal reflectance microscopy," Laryngoscope **109**(10), 1709–1717 (1999).
12. C. J. Koester, J. D. Auran, H. D. Rosskothen, G. J. Florakis, and R. B. Tackaberry, "Clinical microscopy of the cornea utilizing optical sectioning and a high-numerical-aperture objective," J. Opt. Soc. Am. A **10**(7), 1670–1679 (1993).
13. R. A. Drezek, T. Collier, C. K. Brookner, A. Malpica, R. Lotan, R. R. Richards-Kortum, and M. Follen, "Laser scanning confocal microscopy of cervical tissue before and after application of acetic acid," Am. J. Obstet. Gynecol. **182**(5), 1135–1139 (2000).
14. M. Rajadhyaksha, M. Grossman, D. Esterowitz, R. H. Webb, and R. R. Anderson, "In vivo confocal scanning laser microscopy of human skin: melanin provides strong contrast," J. Invest. Dermatol. **104**(6), 946–952 (1995).
15. S. González, R. Sackstein, R. R. Anderson, and M. Rajadhyaksha, "Real-time evidence of in vivo leukocyte trafficking in human skin by reflectance confocal microscopy," J. Invest. Dermatol. **117**(2), 384–386 (2001).

16. G. J. Tearney, R. H. Webb, and B. E. Bouma, "Spectrally encoded confocal microscopy," Opt. Lett. **23**(15), 1152–1154 (1998).
17. C. Boudoux, S. Yun, W. Oh, W. White, N. Iftimia, M. Shishkov, B. Bouma, and G. Tearney, "Rapid wavelength-swept spectrally encoded confocal microscopy," Opt. Express **13**(20), 8214–8221 (2005).
18. D. Yelin, C. Boudoux, B. E. Bouma, and G. J. Tearney, "Large area confocal microscopy," Opt. Lett. **32**(9), 1102–1104 (2007).
19. D. Kang, M. J. Suter, C. Boudoux, H. Yoo, P. S. Yachimski, W. P. Puricelli, N. S. Nishioka, M. Mino-Kenudson, G. Y. Lauwers, B. E. Bouma, and G. J. Tearney, "Comprehensive imaging of gastroesophageal biopsy samples by spectrally encoded confocal microscopy," Gastrointest. Endosc. **71**(1), 35–43 (2010).
20. L. Golan and D. Yelin, "Flow cytometry using spectrally encoded confocal microscopy," Opt. Lett. **35**(13), 2218–2220 (2010).
21. L. Golan, D. Yeheskely-Hayon, L. Minai, E. J. Dann, and D. Yelin, "Noninvasive imaging of flowing blood cells using label-free spectrally encoded flow cytometry," Biomed. Opt. Express **3**(6), 1455–1464 (2012).
22. L. Golan, D. Yeheskely-Hayon, L. Minai, and D. Yelin, "High-speed interferometric spectrally encoded flow cytometry," Opt. Lett. **37**(24), 5154–5156 (2012).
23. T. Wilson and A. R. Carlini, "Size of the detector in confocal imaging systems," Opt. Lett. **12**(4), 227–229 (1987).
24. E. Evans and Y.-C. Fung, "Improved measurements of the erythrocyte geometry," Microvasc. Res. **4**(4), 335–347 (1972).

1. Introduction

The properties of red blood cells (RBCs) are remarkable indicators of the body's physiological condition; their density could indicate anemia or polycythemia, their absorption spectrum correlates with blood oxygenation, and their morphology [1] is highly sensitive to various pathologic states including iron deficiency, ovalocytosis, and sickle cell disease [1, 2]. *In vitro* imaging and analysis of human RBCs have been demonstrated using a conventional blood smear [1], light scattering from an unstained blood smear [3], holographic microscopy [4, 5], photo-acoustic microscopy [6, 7], and confocal microscopy [8]. *In vivo* imaging of RBCs, which is ideal for measuring the physiological properties of the cells within their natural environment, was first demonstrated using reflectance confocal microscopy (RCM) [9, 10] at high-resolution and without the need for fluorescence labeling [9]. RCM has also been demonstrated promising for clinical diagnosis of the oral mucosa [11], cornea [12], uterine cervix [13], and the skin [9, 10, 14], including the characterization of the various skin layers [14], small capillaries [9, 10] and blood cells [10, 15]. Spectral encoding techniques [16] have improved several aspects of RCM by eliminating the need for rapid mechanical beam scanning; spectrally encoded confocal microscopy (SECM) has been shown useful for high frame rate imaging [17] and for imaging large tissue areas [18, 19] using simple, compact imaging probes. By taking advantage of the unidirectional flow of blood within small capillary vessels, spectrally encoded flow cytometry (SEFC) [20], a form of SECM that does not require any beam scanning, has been demonstrated promising for measuring hematocrit and counting white blood cells *in vivo* [21, 22].

A main challenge of all reflectance confocal imaging techniques, including laser-scanning RCM, SECM and SEFC, are interference effects that stem from the high spatial coherence of the focused beam. In most tissue types, these effects are manifested as speckle noise that significantly deteriorates imaging quality. When imaging RBCs, however, the rounded, smooth plasma membrane and the relatively homogenous cytoplasm result in a characteristic appearance of smooth rings and curved features [20]. These features stem directly from the three-dimensional shapes of these cells, and could thus provide invaluable information on their morphology and physiological state. In this work, we develop a numerical model that simulates the confocal reflectance image of a single RBC for various relative axial positions and tilt angles, and compare our results to *in-vitro* SEFC images of flowing RBCs. This method allows us to evaluate the shape of the cells in three dimensions, with potential diagnostic capabilities that are based on accurate measurement of RBC morphology.
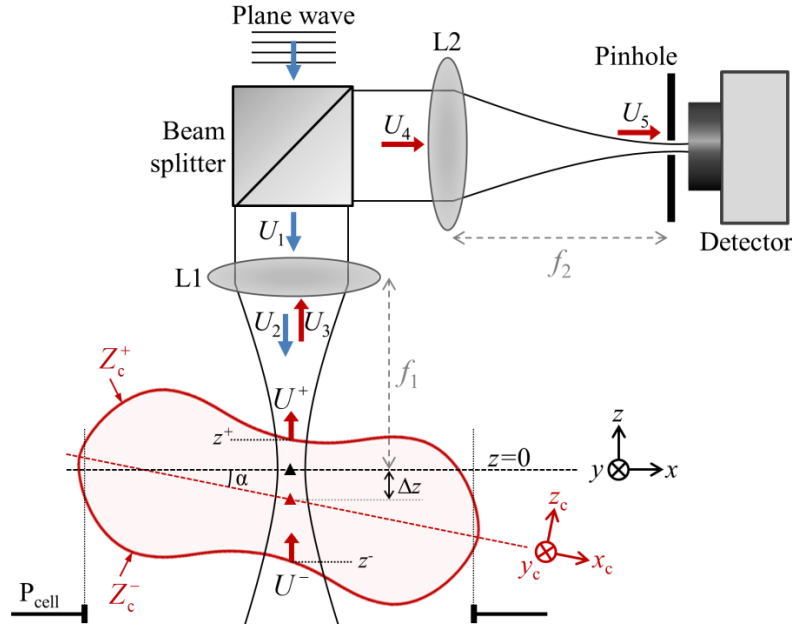
2. Theoretical model and numerical simulation

Fig. 1. Schematic description of the simulated imaging system. L1, L2 – lenses. An image of the cell is acquired by scanning in the lateral x-y plane. The small black and red triangles represent the origin of the optical system and the cell coordinates, respectively.

A schematic of a simplified reflectance confocal imaging system used for our simulation is shown in Fig. 1. According to the Fresnel approximation, the electromagnetic field U_2 after the lens L1 that is illuminated by a monochromatic plane wave U_1, is given by:

$$U_2(x,y,z) = \frac{ie^{ik(f_1-z)}}{\lambda(f_1-z)} \iint U_1 P_{L1} e^{-i\frac{k}{2f_1}(x^2+y^2)} e^{-i\pi\frac{(x-x')^2+(y-y')^2}{\lambda(f_1-z)}} dx'dy', \qquad (1)$$

where λ denotes the wavelength, $k = 2\pi/\lambda$, and f_1 and P_{L1} denote the focal length and the pupil function of the lens L1, respectively. The simulated field amplitude distributions around the focal plane for a water immersion NA = 0.6 objective lens and 840 nm wavelength (Fig. 2(a), blue circles) agrees well with the analytical expression (dashed lines) given by [23]:

$$U(u,v) = \int_0^1 J_0(v\rho) e^{-\frac{i}{2}u\rho^2} \rho d\rho, \qquad (2)$$

where J_0 is zero-order Bessel function, ρ denotes the normalized radial coordinate at the pupil plane, and u and v denote the normalized radial and axial coordinated [23]. A cross sectional (x-z) distribution of the optical field at the focal region is shown in Fig. 2(b) (red colormap).
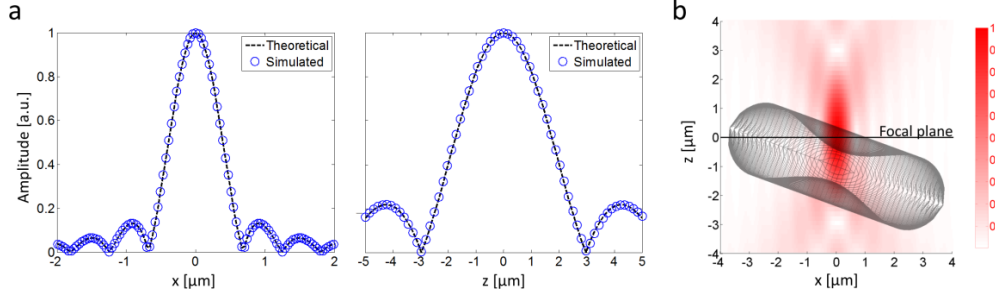
Fig. 2. (a) Lateral (left) and axial (right) field amplitude distributions around the focal point for NA = 0.6 lens and 840 nm wavelength. The simulated fields (blue circles) agree well with theoretical prediction (dashed lines) of Eq. (2). (b) An exemplary x-z cross-section of a simulated cell with a 20° tilt angle and 1 μm below the focal plane, drawn to scale with the cross-sectional field amplitude distribution (red colormap, arbitrary units).

Assuming that the reflections from an RBC originate primarily at the cell's plasma membrane, the reflected wavefront would have phase structures that follow the detailed curvature of the cell membrane. In their work from 1972 [24], Evans and Fung have derived an approximate analytical expression for the front Z_c^+ and back Z_c^- surfaces of an RBC:

$$Z_c^{\pm}\left(x_c, y_c\right) = \left[C_0 + C_2\left(\frac{\sqrt{x_c^2 + y_c^2}}{R_0}\right)^2 + C_4\left(\frac{\sqrt{x_c^2 + y_c^2}}{R_0}\right)^4\right] \cdot (\pm)\sqrt{1 - \left(\frac{\sqrt{x_c^2 + y_c^2}}{R_0}\right)^2}, \quad (3)$$

where R_0, C_0, C_2 and C_4 are specific shape parameters [24] and the subscript 'c' denotes coordinates in the cell's frame of reference. A cross-sectional view of the simulated cell with a 20° tilt angle and axial displacement of 1 μm below the focal plane is shown in Fig. 2(b) (grey meshgrid). For a given lateral position (x_c, y_c) of the illumination optical axis, the waves U^+ and U^- reflected from the front and back cell-medium interfaces, respectively, are given by:

$$U^{\pm}\left(x, y, z^{\pm}; x_c, y_c\right) = U_2\left(x, y, z^{\pm}\right)e^{i2k\left[Z_c^{\pm}\left(x+x_c, y+y_c\right) - Z_c^{\pm}\left(x_c, y_c\right)\right]}P_{cell}, \quad (4)$$

where z^+ (z^-) denotes the axial coordinate of the intersection between the front (back) cell interface and the optical axis, P_{cell} denotes the cell pupil function (see Fig. 1), and the digit 2 at the exponential term results from the roundtrip optical path of the reflected wave. For simplicity, and to avoid numerical artifacts, P_{cell} was slightly smaller than the actual cell size, allowing to neglect reflections from the edges of the cell where angles between the membrane's normal and the optical axis are much larger than the maximum illumination and collection cone angles (26.8°). The wave U_3 reflected back from the cell is thus the sum of U^+ and U^- after propagating a distance of $f_1 - z^+$ and $f_1 - z^-$, respectively, toward the objective lens L1:

$$U_3(x, y) = \frac{ie^{-ik\left(f_1 - z^+\right)}}{\lambda\left(f_1 - z^+\right)}\iint U^+ e^{-i\pi\frac{(x-x')^2 + (y-y')^2}{\lambda\left(f_1 - z^+\right)}} dx'dy' + \frac{ie^{-ik\left(f_1 - z^-\right)}}{\lambda\left(f_1 - z^-\right)}\iint U^- e^{-i\pi\frac{(x-x')^2 + (y-y')^2}{\lambda\left(f_1 - z^-\right)}} dx'dy'. \quad (5)$$

The wavefront U_4 immediately before the lens L2, was calculated by multiplying U_3 by the lens L1 transfer function and propagating a distance f_2 toward the lens L2:

$$U_4(x, y) = \frac{ie^{-ikf_2}}{\lambda f_2}\iint U_3 P_{L1}e^{-i\frac{k}{2f_1}\left(x'^2 + y'^2\right)} e^{-i\pi\frac{(x-x')^2 + (y-y')^2}{\lambda f_2}} dx'dy'. \quad (6)$$

The complex amplitude of the wave U_5, just before the pinhole, was calculated by multiplying the wave U_4 by the transfer function of the lens L2 and propagation by a distance f_2:

$$U_5(x,y) = \frac{ie^{-ikf_2}}{\lambda f_2} \iint U_4 P_{L2} e^{-i\frac{k}{2f_2}(x'^2+y'^2)} e^{-i\pi\frac{(x-x')^2+(y-y')^2}{\lambda f_2}} dx'dy'. \qquad (7)$$

Finally, assuming an infinitesimally small pinhole, the signal measured by the detector was calculated as the wave intensity only at the optical axis, i.e. $I(x_c,y_c) = |U_5(0,0)|^2$. The complete confocal image of the entire cell $I(x_c,y_c)$ was calculated by following Eqs. (4)-(7) for all lateral positions of the imaging beam.

Using our model, confocal images of a single cell were simulated for different axial locations Δz and tilt angles α (Fig. 3). The field symmetry around the focal plane resulted in similar images for positive and negative axial displacements, while the cell's radial symmetry resulted in similar images for positive and negative tilt angles. The simulated images were comprised of various bright rings and curves generated by interference between the two waves reflected from the top and bottom cell-water interfaces. In general, high-brightness images with partial radial symmetry were obtained for $\Delta z<2$ μm and tilt angles below 30°. The relative brightness of the rings varied for different axial shifts: in perfect focus ($\Delta z = 0$) the inner ring was the brightest, while for $\Delta z = 1$ μm the outer ring was more visible. High (>20°) tilt angles resulted in a characteristic bowtie pattern with low-contrast superimposed interference rings. At high tilt angles and large defocusing, the cell appeared as a very dim arc. Additional simulations with different cell morphological parameters revealed (data not shown) that the number of rings or arcs is determined primarily by the overall cell thickness variations; thicker cells with a thin central region have more transitions between constructive and destructive interference, hence a higher number of concentric rings.
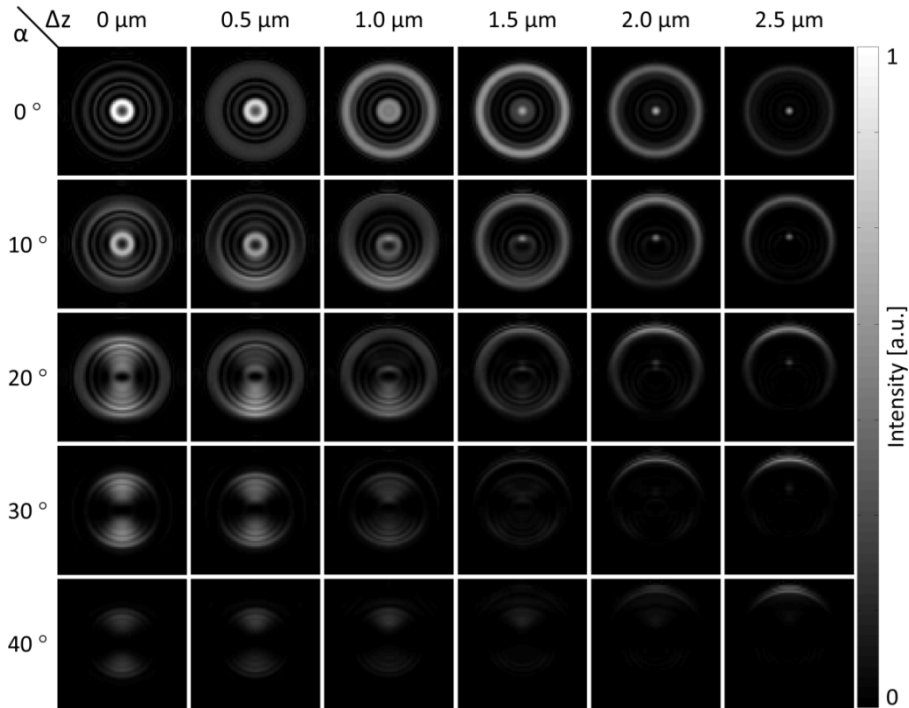

Fig. 3. Simulated RCM images of a red blood cell for different axial positions and tilt angles. Size of each panel is 8 μm × 8 μm. Cell shape is calculated according to Eq. (3) with the parameters reported in Ref [24]: $R_0 = 3.91$ μm, $C_0 = 0.81$ μm, $C_2 = 7.83$ μm, and $C_4 = -4.39$ μm.

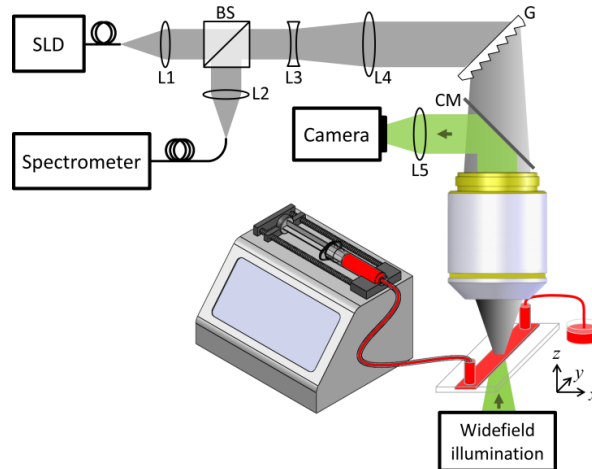## 3. Experiment – cell imaging using SEFC

Fig. 4. Schematic illustration of the bench-top SEFC system for confocal imaging of flowing blood cells. SLD: super-luminescence diode array. L1-5 – lenses. BS – beam splitter. G – transmission grating. CM – cold mirror.

Reflectance confocal imaging of RBCs was conducted using a benchtop SEFC system that was described in detail in previous publications [20, 21]. Briefly, SEFC uses a diffraction grating to separate broadband illumination light into its components across a single transverse line within a flow channel. The spectrally encoded reflections from the flowing cells are collected through the same optical path into the core of a single-mode fiber and directed to a fast spectrometer that decodes the spectral reflectance. As a result, SEFC enables instantaneous confocal imaging of an entire line, resulting in a fast, compact imaging system that does not require any beam scanning. A two-dimensional confocal image of the blood is obtained as the cells flow in the direction (y-axis) perpendicular to the imaged line (x-axis).

Our bench-top SEFC system, schematically illustrated in Fig. 4, comprised of a fiber-coupled broadband super-luminescence diode array (Superlum, 840 nm center wavelength, 53 nm bandwidth), two lenses (−20 mm and 75 mm focal lengths for lenses L3 and L4, respectively) for beam magnification, a transmission diffraction grating (1200 lines/mm, Wasatch photonics) and a × 60 water-immersion NA = 1.2 objective lens. Light reflected
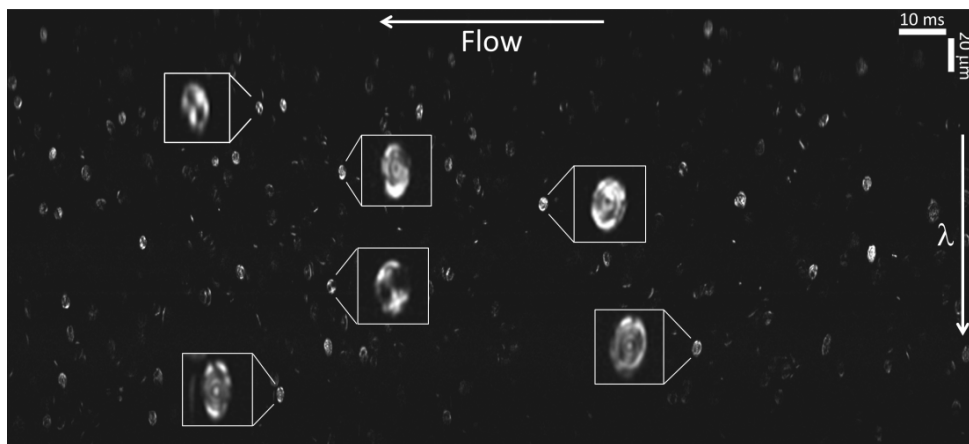

Fig. 5. SEFC image of flowing RBCs. 5 × magnified views are shown next to selected cells.

from the blood cells was propagated back through the same optical path and deflected by a cubic beam-splitter to a fiber-coupled custom-build spectrometer (5000 spectra/s). An additional transmission-mode imaging channel for widefield imaging of the cell flow was comprised of a white-light illumination, a cold mirror (680 nm cut-on wavelength) and a CCD camera (UI-2230SE, IDS). A sample of blood was drawn from a healthy volunteer into a collection tube containing an anticoagulant (K2-EDTA), diluted by adding phosphate buffered saline with 2% bovine serum albumin, inserted into a syringe within a syringe pump (Syringe pump 11 Elite, Harvard Apparatus), and pushed at a velocity of 1 mm/s through a plastic flow channel with a 5 mm x 0.2 mm rectangular cross section (Fig. 4). A typical SEFC image (Fig. 5) of the diluted (1:20) blood within the flow chamber contained scattered spots that correspond primarily to individual RBCs (see magnified rectangles in Fig. 5).

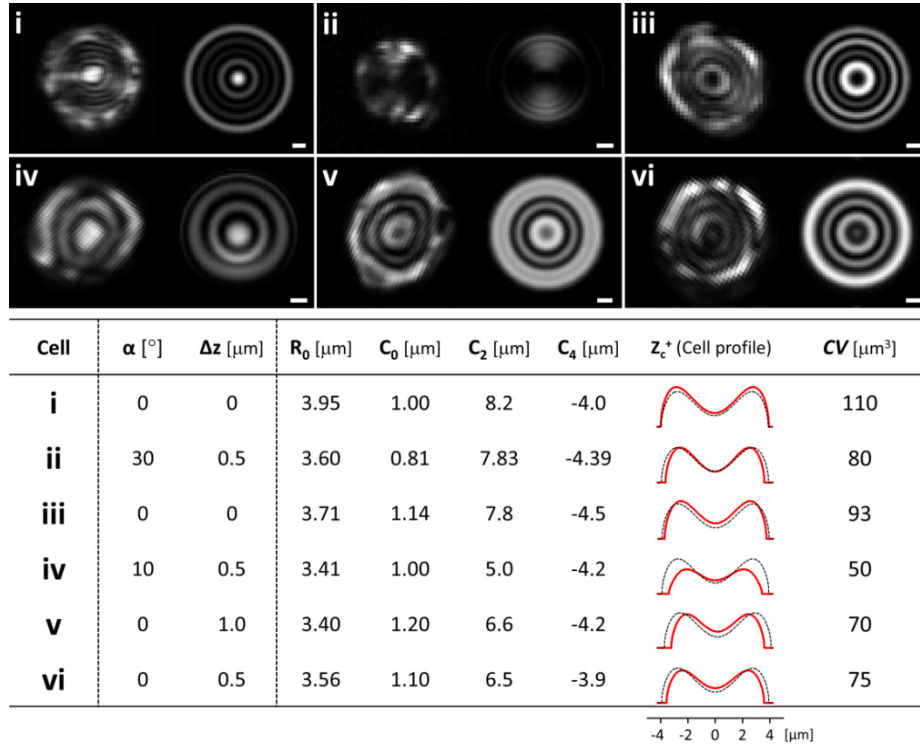| Cell	α [°]	Δz [µm]	R_0 [µm]	C_0 [µm]	C_2 [µm]	C_4 [µm]	Z_c^+ (Cell profile)	CV [µm³]
i	0	0	3.95	1.00	8.2	-4.0		110
ii	30	0.5	3.60	0.81	7.83	-4.39		80
iii	0	0	3.71	1.14	7.8	-4.5		93
iv	10	0.5	3.41	1.00	5.0	-4.2		50
v	0	1.0	3.40	1.20	6.6	-4.2		70
vi	0	0.5	3.56	1.10	6.5	-3.9		75

-4 -2 0 2 4 [µm]

Fig. 6. Top panels: Comparison between six SEFC images of RBCs and simulated confocal patterns that approximate each image. Table: The parameters used to simulate the patterns that correspond to each cell image. Cells' profiles (red curves) are derived using Eq. (3). Dashed curves represent the averaged cell shape in Ref [24]. *CV* – corpuscular volume. Scale bars denote 1 µm.

By varying the different size parameters, it was possible to match the simulated images to SEFC images of the cells. First, the number of concentric rings in the SEFC image was matched in the simulated image by choosing appropriate C_0 and C_2 parameters. Second, adjustment of all C_{0-4} parameters was performed to fine-tune ring width and spacing. Third, a look-up table similar to that in Fig. 3 was constructed, from which the tilt angle α and the axial displacement Δz where chosen that best match the SEFC image. Finally, the cell radius R_0 was set to match the transverse dimensions of the imaged cell. Examples of six cells from our raw SEFC data and their corresponding simulated images are shown in Fig. 6 (top panels). The resulting fit parameters for these cells are presented in the table below, next to the cell profile function Z_c^+ (red curves). The profile of a typical average cell derived in Ref [24]. is plotted by dashed black curves for reference. Assuming rotational symmetry, the

corpuscular volume (*CV*) of each cell was estimated by calculating the volume between the cell's top and bottom interfaces using:

$$CV = 2\pi \int_0^{R_0} 2Z_c^+ (r) r dr. \tag{8}$$

While many of the imaged cells (approximately 70%) showed good agreement with our model and with shapes derived using Eq. (3), the rest of the images exhibited patterns that were inconsistent with the expected cell morphology. Comparison of transmission-mode widefield images with co-registered confocal images of the cells (see two examples in Fig. 7) revealed that such patterns had occurred whenever additional nearby cells were present within the optical path. While some of the distorted cell images could be attributed to abnormal cell morphologies due to sample mishandling, most of the observed irregular patterns were likely caused by wavefront distortions induced by the neighboring RBCs.
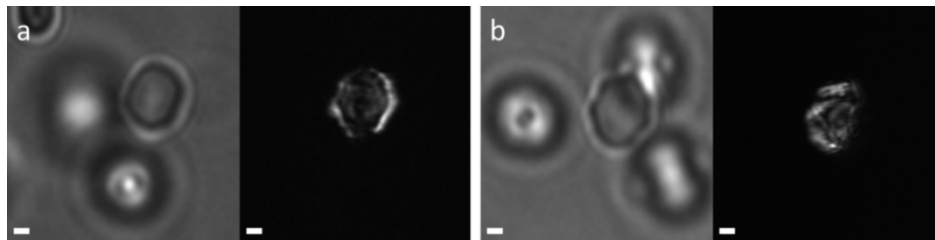

Fig. 7. Comparison between transmission-mode widefield image and co-registered confocal image of the same RBCs. Loss of the characteristic interference rings patterns was most likely due to aberrations induced by nearby out-of-focus cells. Scale bars represent 2 μm.

4. Discussion and conclusion

The unique interference patterns between the front medium-cell and back cell-medium interfaces of a single RBC allow direct sensing of the cell's three-dimensional shape. In this work, we have established a simple approximate model that simulates the reflectance of a tightly focused beam in a confocal microscope configuration. Due to interference between the reflections from the two cell-water interfaces, the resulting images comprise of several concentric rings and curved features. Similar features were also seen in experimental SEFC images of RBCs as they flow in a diluted medium through a flow channel; SEFC is ideal for such comparison as it allows confocal imaging of individual cells without a nearby glass [3] interface that would modify the interference patterns or disturb the natural cell shape. By using this approach, it may be possible to compute the volume of each individual cell and consequently the mean corpuscular volume, which is an important and clinically useful RBC index. This method could also be used for distinguishing between healthy and abnormal RBCs in autosomal recessive blood diseases such as thalassemia and sickle cell anemia.

At present, the presented method has some limitations due to the simplified simulation model and the wide diversity of cell shapes. The Fresnel approximation is valid for wavefronts propagating with relatively small angles; the approximation is good for NA<0.6, remains practical (up to 10% error in PSF lateral dimensions) for 0.6<NA<0.9, and generally fails for higher numerical apertures. Our experimental SEFC system utilized a high-NA (1.2 water immersions) objective lens; however, its measured lateral and axial resolutions (0.7 μm and 1.5 μm, respectively) were much lower than expected, most likely as the beam diameter was smaller than the back aperture of the objective lens. Based on these parameters, we assumed that the effective NA of the imaging experiment was approximately 0.6, within the validity range of the Fresnel approximation. High-NA systems would most likely require a more sophisticated optical model for error-free morphological measurements; however, such system would probably exhibit less interference effects between the two cell interfaces due to the shallow depth of field. The wide diversity of cell shapes makes effective matching

between experimental and theoretical images challenging; while the errors in the approximated cell profiles and volumes (Fig. 6) were difficult to estimate in this work due to the manual matching procedures, future development of automatic algorithms may improve processing speed and accuracy and reduce measurement errors. Another limitation of the system is its sensitivity to the presence of other cells within the optical path, which distort the beam wavefront and modify the resulting interference patterns. This issue could be addressed by using a highly diluted blood and/or by neglecting measurements of cells that do not show the expected characteristic patterns. Finally, the presented method may not be suitable for *in vivo* experiments [21] due to the high density of cells within blood vessels and the degrading effects of the scattering tissue and vessel walls on the beam wavefront.

In summary, a model for simulating reflectance confocal images of RBCs has been demonstrated, revealing the relation between cell morphology and the resulting interference patterns. By comparing the simulated cell images to experimental confocal images, the model could be useful for measuring individual cell morphology and for estimating its volume. Potential applications for this technology include *in vitro* measurement of the mean corpuscular volume of RBCs and diagnosis of hematological disorders such as thalassemia and sickle cell anemia.

Acknowledgments